Science of the Total Environment 912 (2024) 169053

Contents lists available at ScienceDirect

Science of the Total Environment

journal homepage: www.elsevier.com/locate/scitotenv

A decadal atmospheric ammonia reanalysis product in China

Bufan Xu, Jianbing Jin *, Li Fang, Mijie Pang, Ji Xia, Baojie Li, Hong Liao *

Joint International Research Laboratory of Climate and Environment Change, Jiangsu Key Laboratory of Atmospheric Environment Monitoring and Pollution Control, Jiangsu Collaborative Innovation Center of Atmospheric Environment and Equipment Technology, School of Environmental Science and Engineering, Nanjing University of Information Science and Technology, Nanjing, Jiangsu, China

HIGHLIGHTS

- Ammonia reanalysis was made through assimilating IASI observations into a model.
- Independent evaluation indicates our reanalysis has high quality.
- The reanalysis unveils spatial and temporal patterns of NH3 concentrations in China.
- Ammonia reanalysis product is valuable in the future NH_3 control in China.

GRAPHICAL ABSTRACT

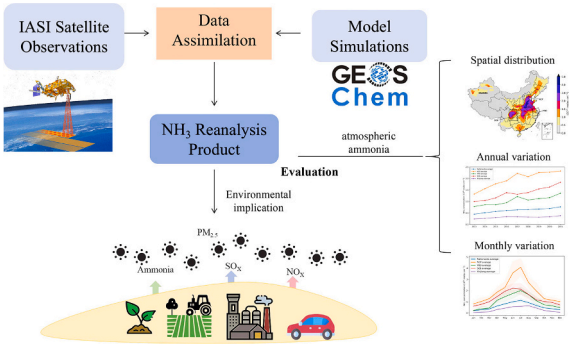

ARTICLE INFO

Editor: Jianmin Chen

Keywords:
Atmospheric ammonia
Data assimilation
IASI
Reanalysis

ABSTRACT

Atmospheric ammonia has great environmental implications due to its important role in ecosystem and nitrogen cycle, as well as contribution to formation of secondary particles. China is recognized as a hotspot of NH_3 pollution owing to agricultural and livestock intensification. In the quest to achieve a comprehensive understanding of atmospheric ammonia load and to quantify its environmental impacts in China, relying solely either on existing measurements or on model simulations falls short. Their limitations, either in spatial coverage and integrity or in data quality, fails to meet the needs. Available reanalysis products exhibit a marked deficiency in ammonia data. We therefore aim to propose an integrated ammonia reanalysis product in China, adeptly melding satellite observations from the Infrared Atmospheric Sounding Interferometer (IASI) NH_3 retrievals with chemical transport model simulation, capitalizing on the robust Ensemble Kalman Filter (EnKF) data assimilation methodology. The product is validated in high quality via the comparison against independent measurements from ground monitoring stations. Spanning a decade from 2013 to 2022, our reanalysis uncovers not just the spatial intricacies of NH_3 concentrations but also their temporal dynamics. Our findings pinpointed the spatial disparities in atmospheric ammonia intensities, highlighting regional hotspots in the NCP, SCB, and Northeast China, and identified annual and seasonal patterns. Our research provides crucial insights for shaping future NH_3 pollution prevention and control strategies in China.

* Corresponding authors.
E-mail addresses: jianbing.jin@nuist.edu.cn (J. Jin), hongliao@nuist.edu.cn (H. Liao).

https://doi.org/10.1016/j.scitotenv.2023.169053
Received 16 October 2023; Received in revised form 30 November 2023; Accepted 30 November 2023
Available online 12 December 2023

1. Introduction

Atmospheric ammonia (NH_3), being the most abundant base in the atmosphere, has significant environmental implications owing to its crucial role in the ecosystem and the global nitrogen cycle, as well as its contribution to the formation of secondary particles (Sutton and Fowler, 2002; Sutton et al., 2008). The predominant source of NH_3 emissions stems from the agricultural sector, including livestock rearing and the application of ammonia-based fertilizers (Dong et al., 2023; Liu et al., 2023). Other contributors to ammonia emissions include industrial activities, vehicular exhaust, and the volatilization of ammonia from soils and oceans (Behera et al., 2013). A substantial amount of atmospheric NH_3 results in excessive nitrogen deposition, which triggers a series of environmental issues. These include the reduction in biodiversity, soil acidification, and degradation of water quality (Ti et al., 2019).

China is recognized as a hotspot of NH_3 pollution owing to agricultural and livestock intensification since 1980 (Warner et al., 2016; Zhan et al., 2020; Zhang et al., 2021). To scientifically address NH_3 pollution in China, an accurate assessment of the atmospheric loading and emissions is essential. Lots of efforts have paid to understand the scale and pattern of ammonia emissions. The Global Atmospheric Research Emissions Database (Crippa et al., 2018), the Community Emissions Data System (CEDS) (Hoesly et al., 2018), and regional NH_3 inventories over China (Huang et al., 2012; Kang et al., 2016; Xu et al., 2016; Zhou et al., 2016; Zhang et al., 2018) have developed global/regional emissions inventory and quantifying the spatial and temporal distributions of ammonia sources. Together with these datasets, several chemical transport models (CTMs), like the Goddard Earth Observing System Chemistry (GEOS-Chem) model (Walker et al., 2012) and WRF-Chem (Li et al., 2021), are capable of simulating the physical and chemical life cycles of atmospheric ammonia. Nonetheless, their performance is limited to some extend due to the model uncertainties, especially in the emission inventories. Because there are a wide array of fluctuations in emission factors and the challenges in garnering consistent and all-encompassing data across a vast nation like China. For example, Zhou et al. (2016) used a bottom-up method to estimate Chinese annual farmland NH_3 emission in 2008, which was about 3.96 Tg N yr^{-1}. It was notably different from the approximation 2.89 Tg N yr^{-1} in Intergovernmental Panel on Climate Change (IPCC) Tier-1 guidelines.

In addition to the model simulation, measurements from the ground-based stations and remote sensing platforms are regarded as the most precise quantitative method for evaluating the atmospheric ammonia (Liu et al., 2022). The Ammonia Monitoring Network in China (AMoN-China) gained the largest popularity for the invaluable observations. However, it consists of only 53 monitoring sites across the whole country, and its observational campaign lasted just one year from 2015 to 2016 (Pan et al., 2018). These stations mainly focus on urban areas or particular hotspots, and overlook vast rural and remote regions which are significant sources. This hindered a comprehensive spatial assessment.

The rapid advancements in atmospheric remote sensing have made the NH_3 monitoring on a global scale feasible. Satellite-based remote sensing instruments, like the Tropospheric Emission Spectrometer (TES) (Beer et al., 2008), Infrared Atmospheric Sounding Interferometer (IASI) (Clarisse et al., 2009), and Crosstalk Infrared Sounder (CrIS) (Shephard and Cady-Pereira, 2015), offer invaluable insights into ammonia dynamics (Ge et al., 2020) and are now widely employed in ammonia nitrogen analysis. However, satellite ammonia retrieval products provide the column-integrated concentration quantities, instead of measuring the three dimensional characteristics directly. The ammonia loading at the surface layer that strongly reflects the emission intensity are also not available. Meanwhile, high data missing vacancies are inevitable due to the cloudy scene and other retrieval errors. Despite their significant roles in characterizing the atmospheric ammonia load, using only the measurements is not sufficient to obtain a complete four-dimensional insight into the ammonia spread, because either the measurements do not cover all areas (surface network), or observe only vertically integrated quantities with highly data missing ratio (satellite data).

In light of these limitations, reanalysis data has emerged as a more reliable source for studying the earth dynamics. Reanalysis, though a nascent field, traces its roots back to the utilization of meteorological data gathered for the Global Weather Experiment (GWE) in 1979 (Hinzpeter et al., 2011). Unlike weather analyses archived from operational forecasting systems, a reanalysis is generated using a data assimilation system to combine the forecast model and available measurements, ensuring it remains less affected by model uncertainties (Kalnay et al., 1996). Atmospheric reanalyses have seen improvements across generations. Notable global reanalyses come from JMA (Onogi et al., 2007), NCEP (Saha et al., 2010), ECMWF (Dee et al., 2011), NASA (Rienecker et al., 2011), and NOAA-CIRES (Compo et al., 2011). These advancements are often attributed to techniques like data assimilation (Ebita et al., 2011). By integrating simulation models and observational data, data assimilation surpasses the reliance on either method alone for examining the atmospheric ammonia cycle. This approach serves as a bridge between observations and modeling, enabling adjustments to parameters or states within acceptable limits, leading to simulations that closely match measurements (Kalnay, 2002).

These reanalysis have been providing fundamental datasets for climate researches. However, these reanalysis products are commonly deficient in ammonia data, a shortcoming recognized as a significant gap in atmospheric research. According to a study by Paulot et al. (2015), this absence of a three dimensional continuous and accurate ammonia data impedes our understanding of nitrogen cycles and atmospheric chemistry, especially regarding the formation of aerosols. A study by Wang et al. (2018) notes the challenges in obtaining reliable ammonia dataset in China, which has unique industrial and agricultural practices influencing ammonia emissions. The scarcity of data and targeted research on China's atmospheric ammonia levels underscores a significant opportunity for further exploration. Our research endeavors to bridge this knowledge gap via proposing a reanalysis data product across China. This innovative system harmoniously blends satellite observations from the IASI NH_3 dataset with model data, employing the Ensemble Kalman Filter (EnKF) data assimilation method. The timeline of our reanalysis extends from 2013 to June 2022. The objectives of this study are to describe how ammonia IASI data can be assimilated into GEOS-Chem and to explore the validity and accuracy of this approach. The reanalysis product is then utilized to analyze the spatial and temporal characteristics of NH_3 concentration on a national scale over the past decade. The proposed reanalysis data product system is poised to enhance our understanding of the variations in atmospheric ammonia concentrations across China, thereby facilitating a comprehensive assessment of its environmental implications.

The structure of this article is organized as follows: Section 2.1 offers an overview of ammonia simulation from GEOS-Chem and the IASI observations. Section 2.2 introduces the EnKF assimilation methodology. Section 3 delves into reanalysis data validation and provides a spatio-temporal analysis of atmospheric loading in China. Finally, Section 4 concludes the paper with a summary of our findings and outlines future directions.

2. Data and methods

2.1. Ammonia observations and simulation

2.1.1. Satellite IASI NH_3

The IASI, an infrared Fourier transform sounder, is equipped on the Sun-synchronous Meteorological Operational satellite series A/B/C (Metop-A/B/C), launched in 2008, 2012, and 2018 respectively. Each of these IASI devices captures bi-daily data on a spectrum of atmospheric contaminants during its flyby between 09:30 and 21:30 at local time. Offering a notable spatial precision of 12 km at its nadir, the IASI boasts a swath dimension of 2 × 1100 km (Clerbaux et al., 2009).

Enhancements have been made to the ammonia retrieval methodology of IASI steadily. For our research, we employed the most recent IASI release (version 3) (ANNI-NH_3-v3R-ERA5) from the Metop-A/B/C satellites. This edition draws from the foundational knowledge of its predecessors and integrates enhancements in neural network retrieval as detailed by Franco et al. (2019).

In spite of advancements in NH_3 column retrieval from satellite data, significant fluctuations in measurement error persist, ranging from as low as 5 % to exceeding 1000 % (Van Damme et al., 2017). Given the elevated levels of uncertainty inherent in infrared-based retrievals, coupled with a high incidence of data vacancies over cloudy regions, IASI-derived products are generally deemed inadequate for real-time ammonia surveillance, though their monthly aggregates meet required standards (Ge et al., 2020). In a similar vein, monthly averages across the 0.5°×0.625° GEOS-Chem grid cells were computed using raw data from the ANNI-NH_3-v3R-ERA5 dataset. Concurrently, irrational observed values (<0) were omitted from the monthly mean computations. Snapshots of the IASI observations for assimilation at four different seasons are showcased in Fig. 1(a.1)–(a.4).

This study aimed to calculate the 3D continuous ammonia field that best fit both the IASI ammonia column data and the GEOS-Chem model simulation. The observation error covariance matrix that quantifies the penalty of the IASI measurements is essential in the data assimilation as will be described later in Section 2.2. While assessing the uncertainty of the monthly averaged ammonia measurements on a grid, both the instrument error, denoted as $\sigma^{\text{instrument}}$, and representational errors, denoted as $\sigma^{\text{representing}}$, were taken into account. The average uncertainty derived from the IASI product served as the instrument error $\sigma^{\text{instrument}}$, while the variability (standard deviation) in observation samples used to derive the grid average denotes the representation error $\sigma^{\text{representing}}$. Consequently, the cumulative uncertainty, $\sigma^{\text{integrated}}$, which encapsulates the IASI ammonia product error to depict atmospheric ammonia intensity, was computed as:

$$\sigma^{\text{integrated}} = \left\{ \left(\sigma^{\text{instrument}}\right)^2 + \left(\sigma^{\text{representing}}\right)^2 \right\}^{0.5} \quad (1)$$

Snapshots of the IASI uncertainty for assimilation are showcased in Fig. 1(b.1)–(b.4).

2.1.2. GEOS-Chem model

The GEOS-Chem model version 13.3.3 is a three-dimensional chemical transport model. This model, pioneered by Harvard University, has garnered widespread acclaim for its role in atmospheric investigations (Eastham et al., 2014). This study utilized its nested regional model in Asia. The global scale had a resolution of 2° latitude by 2.5° longitude and was sampled every 3 h, providing the boundary conditions. The nested domain covered 72° – –136°E and 17.5° – –54°N with a resolution of 0.5° latitude by 0.625° longitude. The model used the Modern-Era Retrospective Analysis for Research and Applications, version 2 (MERRA-2) meteorological field (Gelaro et al., 2017)

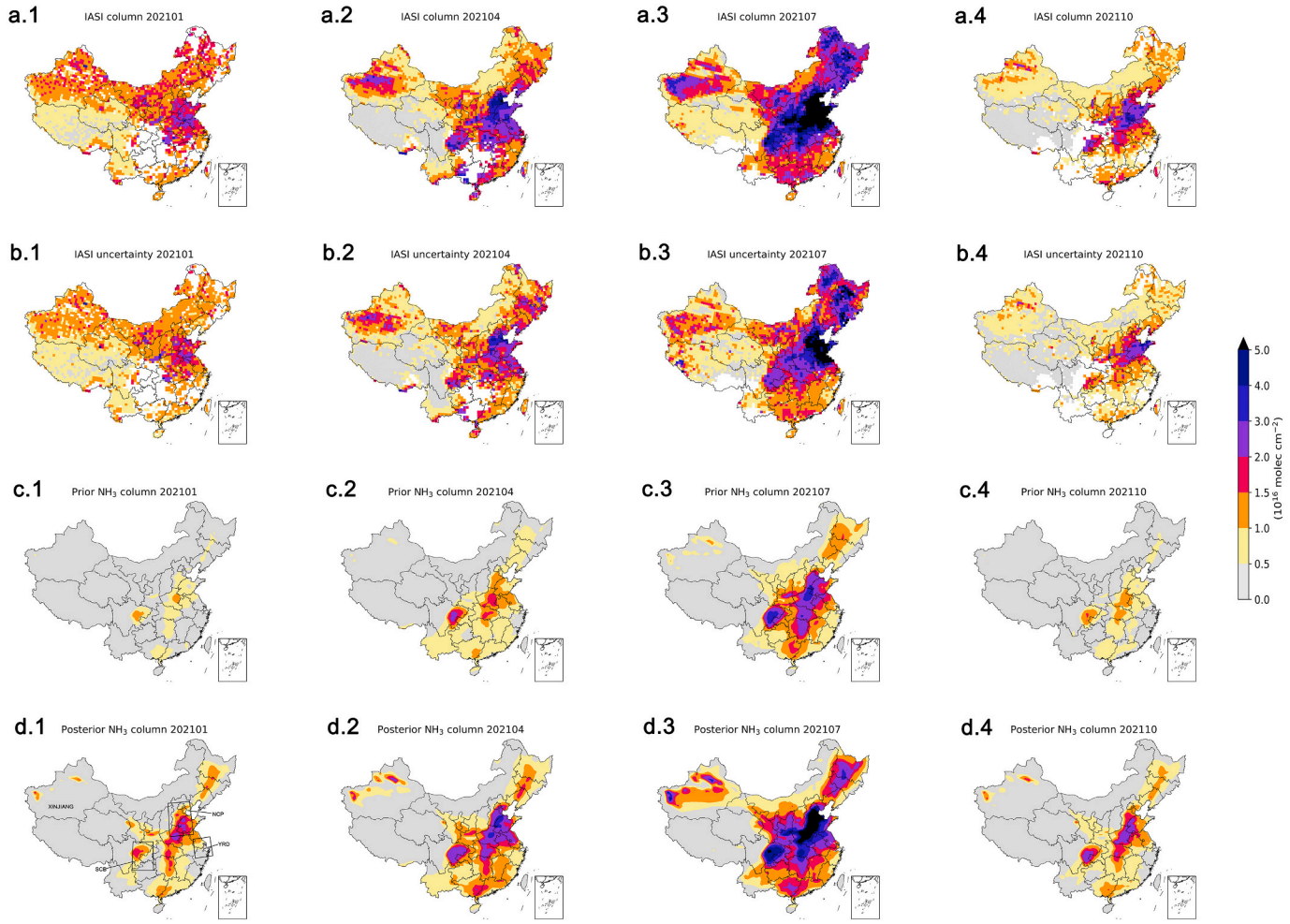

Fig. 1. Scenarios of the monthly ammonia column concentrations in January, April, October, and December 2021. IASI observations (a.1)–(a.4), IASI observational uncertainties (b.1)–(b.4), GEOS-Chem prior simulations (c.1)–(c.4), the posterior ammonia column concentration, by assimilating IASI into GEOS-Chem, is in (d.1)–(d.4).

with a 6-month spin-up. Internally, GEOS-Chem is supported by a fully coupled aerosol-ozone-NO_x-hydrocarbon chemistry representation (Park et al., 2004). The wet deposition scheme for soluble aerosols and gases was described in Liu et al. (2001) and the dry deposition scheme was described in Zhang et al. (2001). Dry deposition calculation in GEOS-Chem follows a standard resistance-in-series model (Wesely, 2007), while wet deposition includes both convective updraft and large-scale precipitation scavenging (Jacob, 1999). The GEOS-Chem outputs of NH_3 concentrations include 47 layers from the ground to the top of the atmosphere, which were used to capture NH_3 vertical profiles.

To ensure regional specificity, the default anthropogenic emissions including the ammonia source across China were from the Multi-resolution Emission Inventory for China (MEIC, www.meicmodel.org, last access: August 1, 2022). The ammonia simulation driven by MEIC inventory is referred to as the prior simulation. As aforementioned, the major error source in the ammonia simulation is attributed to the uncertainty in the emission approximation. The ensemble ammonia model are therefore forwarded with the consistent GEOS-Chem but perturbed ammonia emission inventory as will be explained in Section 2.2. They represented the potential spread of the four dimensional ammonia characteristics.

2.1.3. Surface ammonia measurements

These surface ammonia concentration observations for validating our reanalysis are from two sources: the National Nitrogen Deposition Monitoring Network (NNDMN) (Xu et al., 2015) established by the China Agricultural University, and the Ammonia Monitoring Network of China (AMoN-China) (Pan et al., 2018), which is based on the Chinese Ecosystem Research Network. NNDMN consists of 43 ground stations, covering cities, farmland, coastal areas, forests and grasslands. This network provides 2013 to 2014 monthly records of surface NH_3 concentrations using harmonized protocols and measurement techniques. The AMoN-China has 53 monitoring stations and records NH_3 concentrations on a monthly basis. A year-round observational campaign (September 2015 to August 2016) was conducted to capture the spatial variability of atmospheric ammonia. The measurement protocol was based on a diffusion technique, similar to that used by NNDMN. Both NNDMN and AMoN-China monthly observations are treated as the independent observations for evaluating our reanalysis.

2.2. Data assimilation system

The assimilation methodology rooted in Bayesian theory aims to enhance prediction and estimation accuracy by integrating observational data with numerical models. This study employed the Ensemble Kalman Filter (EnKF), originally introduced by Evensen (1994). Similar to other assimilation algorithms, this system fundamentally relies on Bayesian theory to calculate the optimal posterior that best fitting the two prior distributions, quantified by their respective covariance matrices (Evensen et al., 2022).

We assume that the main uncertainty of the ammonia simulation is in the prior emission inventory. Although other model procedures such as chemistry reactions and ammonia removal are uncertain too, they are assumed to be of less importance than the loading of ammonia emission as we did in Jin et al. (2023). This assumption could be seen as a first step toward a system that takes into account other uncertainties too but that probably requires additional information such as deposition flux of NH_3 which are currently not available.

To initiate the assimilation, we generate ensemble simulations ($N = 16$) via the GEOS-Chem model $\mathscr{M}$ with perturbed emission inventories $[f_1,\ldots,f_N]$. These ensemble emission inventories are generated randomly following the prior MEIC model and the background error covariance used in our recent study (Jin et al., 2023). In that study, the uncertainty in the ammonia simulation was assumed to arise from errors in the emission inventory, and can be compensated using a spatially varying tuning factor α:

$$f(i) = f_N(i)\cdot\alpha(i) \tag{2}$$

in here $f_N(i)$ denotes the ammonia emission rate i the given grid cell i. The α values are defined to be random variables with a mean of 1.0 and a standard deviation $\sigma_\alpha = 0.2$. This empirical value was found to provide sufficient spaces for resolving the observation-minus-simulation errors. With these perturbed emission fields, the ensemble ammonia simulation is forwarded as:

$$\left[x_1^f,\ldots,x_N^f\right] = \left[\mathscr{M}(f_1),\ldots,\mathscr{M}(f_N)\right] \tag{3}$$

Here, $\overline{x}^f \in \mathbb{R}^n$ represents the ensemble mean of $x_i^f \in \mathbb{R}^n$, n represents the dimensions of the gridded GEOS-Chem model. The ensemble perturbation $X^{'} \in \mathbb{R}^{n\times N}$ is calculated via:

$$X^{'} = \left[x_1^f - \overline{x}^f,\ldots,x_N^f - \overline{x}^f\right] \tag{4}$$

The background covariance matrix $\mathbf{P}$ for representing the ammonia three concentration uncertainties are approximated through:

$$\mathbf{P} = \frac{1}{N-1}\,\mathbf{X}^{'}\,\mathbf{X}^{'\mathrm{T}} \tag{5}$$

The posterior simulation, denoted as x_a^f, is updated following EnKF:

$$x_a^f = \overline{x}^f + \mathbf{K}\left(y - \mathscr{H}\overline{x}^f\right) \tag{6}$$

Here, $y \in \mathbb{R}^m$ represents the observed NH_3 column concentrations from IASI, $\mathscr{H} \in \mathbb{R}^{n\times m}$ is the linear operator mapping the gridded GEOS-Chem simulation into the IASI observational space, and $\mathbf{K}$ stands for the Kalman gain which is computed following Eq. (7):

$$\mathbf{K} = \mathbf{P}\mathscr{H}^{\mathrm{T}}\left(\mathscr{H}\mathbf{P}\mathscr{H}^{\mathrm{T}} + \mathbf{O}\right)^{-1} \tag{7}$$

$\mathbf{O} \in \mathbb{R}^{m\times m}$ represents the observational error covariance matrix, and the diagonal elements stores the square of the IASI uncertainty calculated in Section 2.1.1.

Despite its capability to approximate covariance of the spatial dynamics using the limited ensemble CTMs, the classic EnKF has some limitations, primarily its reliance on a relatively small ensemble size (N) compared to the high model dimensions (n) for estimating the background error covariance $\mathbf{P}$ dynamics (Houtekamer and Mitchell, 2001). To mitigate spurious spatial correlations within $\mathbf{P}$, a widely adopted distance-dependent localization scheme proposed by Lei and Anderson (2014) is used. The localization is executed by element-wise multiplication of a local support matrix $\mathbf{L}$ with $\mathbf{P}$, as described by the equation:

$$\mathbf{P}^{\mathrm{local}} = \mathbf{P} \circ \mathbf{L} \tag{8}$$

The individual elements of the local support matrix $\mathbf{L}$ are computed using the expressions presented in Eq. (9) and Eq. (10). Specifically:

$$\mathbf{L}_{i,j} = \begin{cases} 1 - \frac{5}{3}\mathbf{S}_{i,j}^2 + \frac{5}{8}\mathbf{S}_{i,j}^3 + \frac{1}{2}\mathbf{S}_{i,j}^4 - \frac{1}{4}\mathbf{S}_{i,j}^5, & \mathbf{S}_{i,j} < 1 \\ -\frac{2}{3}\mathbf{S}_{i,j}^{-1} + 4 - 5\mathbf{S}_{i,j} + \frac{5}{3}\mathbf{S}_{i,j}^2 + \frac{5}{8}\mathbf{S}_{i,j}^3 - \frac{1}{2}\mathbf{S}_{i,j}^4 + \frac{1}{12}\mathbf{S}_{i,j}^5, & 1 \le \mathbf{S}_{i,j} < 2 \\ 0, & \mathbf{S}_{i,j} \end{cases} \tag{9}$$

$$\mathbf{S}_{i,j} = \frac{\mathbf{D}_{i,j}}{L_{thres}} \tag{10}$$

Here, $\mathbf{S}_{i,j}$ represents the spatial distance between grid cells i and j, while L_{thres} is the localization distance threshold. Notably, the correlation value $\mathbf{L}_{i,j}$ decreases with increasing distance. For this study, we conducted a comparative analysis of different empirical localization choices (100, 300, 500 and 800 km). The comparison revealed that the assimilation process yielded the most accurate posterior estimate against the IASI observations when localization was set at 300 km. This threshold is

used for the assimilation reanalysis throughout this paper.

3. Reanalysis evaluation

Using the IASI observations, the GEOS-Chem prior simulation and the EnKF data assimilation described above, the three dimensional reanalysis of atmospheric ammonia are generated and freely accessible via Zenodo (doi:https://doi.org/10.5281/zenodo.8427519). This dataset provides monthly data from January 2013 to June 2022, encompassing a geographic range spanning from 72° to 136° longitude and 17.5° to 54° latitude, and offering a horizontal resolution of 0.5° latitude by 0.625° longitude. Our reanalysis product is capable of providing a more comprehensive and accurate description of gas concentrations in China. To augment the rigor of our dataset, the reanalysis is compared against the assimilated IASI measurement in Section 3.1, independent ground ammonia concentration observations in Section 3.2 as well as a widely-used operational reanalysis Copernicus Atmosphere Monitoring Service (CAMS) in Section 3.3.

3.1. Evaluation with the IASI product

Fig. 1 presents scenarios of the monthly ammonia column concentration either from the IASI product (a.1–a.4), or from the prior GEOS-Chem simulation (c.1–c.4) and posterior results (d.1–d.4). These four snapshots are collected in January, April, July and October in 2021. They are to encapsulate the variances and distinct features of the assimilated observations and simulations at different seasons in China, ensuring the robustness and comprehensiveness of our dataset.

The comparison between the IASI dataset and prior/posterior simulation shown in Fig. 1 shows the consistent distribution of ammonia loading in most of the regions. All three data sources indicated high ammonia concentrations are present in the North China Plain (NCP), and reached the peak in Summer (July) with the column concentration exceeding 3×10^{16} molec cm^{-2} in all the three cases. The seasonal variation will be discussed in details in the following Section 4.3. However, the prior model exhibits deficiency particularly in the central regions of NCP, the Sichuan Basin (SCB), and the Yangtze River Delta (YRD), such as the metropolis of Beijing in NCP. It underestimates ammonia loading compared to IASI observations in generally, and fails to reproduce the reality over these heavily-polluted areas. This is mainly caused by the underestimation of emission intensity (up to 50 % in NCP as indicated by Jin et al. (2023)). In contrast, the posterior is much nudged and better fits the IASI observations. In the Xinjiang region, there is a clear difference between the prior ammonia concentrations from the GEOS-Chem model and the measurements. Specifically, the IASI data showed that the Xinjiang region exhibited mild ammonia pollution in all months, whereas the prior GEOS-Chem model appeared to ignore the ammonia pollution in this region, showing negligible ammonia. In contrast, the reanalysis result is nudged correctly through assimilation. The hotspots of ammonia loading in NCP, SCB, YRD as well as Xinjiang are successfully reproduced.

Fig. 2 presents the scatter plot of the IASI and the simulated prior/posterior column concentrations, they are to further highlight and visualize the improvement of using the assimilation. In the comparison against the assimilated IASI measurement, the prior simulations result in the Pearson correlation coefficient (r), 0.50, 0.72, 0.75 and 0.76, and root mean square error (RMSE) of 1.15×10^{16} molec cm^{-2}, 1.01×10^{16} molec, 1.84×10^{16} molec cm^{-2} and 1.80×10^{16} molec cm^{-2} in the four tested months. The performance were steadily improved except in the January, with the r increased to 0.80, 0.85 and 0.80 and RMSE declined to 0.73×10^{16} molec cm^{-2}, 1.19×10^{16} molec cm^{-2} and 0.58×10^{16} molec cm^{-2} in the three warm months. The least improvement is observed in the January, the RMSE slightly decreased to 1.01 μg/m^3 while r stayed at the same level (0.5). Meanwhile, the scatter plot in Fig. 2(a.1) and (b.1) clearly showed that most of the reanalysis ammonia column concentration are not modified. To gain a deep understanding of the limitation, we reviewed the IASI observations and their uncertainty as shown in Fig. 1. The IASI observation values and its uncertainty are in a positive proportional relationship. Those high IASI values are generally assigned with higher observational errors, such as the IASI ammonia loading in the most polluted summer season returns the highest average uncertainty as shown in Fig. 1(a.3) and (b.3). However, relatively higher uncertainties are present in January especially in the northern areas compared to the April and October cases which are bothered with more severe ammonia. This is due to the fact that the IASI retrieval algorithm is highly sensitive to temperature inputs (Bouillon et al., 2020). It also leads us to less believe these observations at the cold time, and small penalty in the Kalman gain calculation in Eq. (7). Compared to other optimizing methods that calculates the estimation to solely fit the measurements, data assimilation aims to calculate the posterior that fit both the observations and prior, and avoids to be mislead by low-quality measurements. This finally account for that the posterior are less estimated through assimilation the IASI in the cold time.

3.2. Evaluation with the ground NH_3 observation

Our reanalysis were further evaluated against the independent surface ammonia concentration data obtained from AMoN-China and (NNDMN). Fig. 3 displays a comparison between the prior and posterior surface ammonia concentrations simulation at the month of August, specifically chosen to demonstrate the advantages of employing our reanalysis in reproducing surface ammonia concentrations. The overall performance of the reanalysis product against the surface ammonia measurements is presented in Fig. 4.

The posterior surface ammonia concentration in Fig. 3(a.1) presents the very similar distribution to the prior one shown in Fig. 3(b.1), while the regional features are modified correctly. The surface ammonia intensity were underestimated in general in the initial simulation. For instance, the ground monitoring stations indicated the surface ammonia concentration exceeds 16 μg/m^3 over the hotspots of the NCP, while they are around 8 to 12μg/m^3 in the pure model simulation. This underestimation has been corrected in the reanalysis product through assimilating the IASI column measurements. The scatter plot in Fig. 3 (a.2) and (b.2) showed an improvement in the negative bias of the simulation results of surface ammonia concentration in August 2016, with root mean square errors decreasing from 11.06μg/m^3 to 10.05μg/m^3. The improvement obtained in surface concentration simulation is less than that results in ammonia column concentration modeling, and there is still a negative bias remained. One potential reason for this situation is that our simulation represents the average ammonia load of coarse grid cells (0.5°×0.625°). However, the surrounding atmospheric ammonia measured by ground monitoring points may differ significantly with the grid. When comparing the coarse-grid simulation against the ground observations, representation errors are inevitable.

Fig. 4 presents the scatter plots of observed NH_3 surface concentrations with both a priori and a posteriori modeling results spanning from 2013 to 2016. It is clearly illustrated that the a prior model underestimated the surface ammonia loading, and the posteriors display an upward trend in the scatter display with less bias. In term of the RMSE metrics, the comparisons show the performance of our reanalysis surpass consistently the prior across all four years, with RMSE values reduced from 5.32μg/m^3 (2013) to 5.11μg/m^3, 6.17μg/m^3 (2014) to 5.54μg/m^3, 7.29μg/m^3 (2015) to 6.49μg/m^3 and 8.31μg/m^3 (2016) to 7.45μg/m^3, respectively. The independent evaluation give us the confidence that our reanalysis product offer a more representative depiction of the reality of the atmospheric ammonia.

3.3. Comparison with CAMS

Other reanalysis products are accessible for atmospheric ammonia analysis, such as the CAMS product. Fig. 5 plots the monthly column

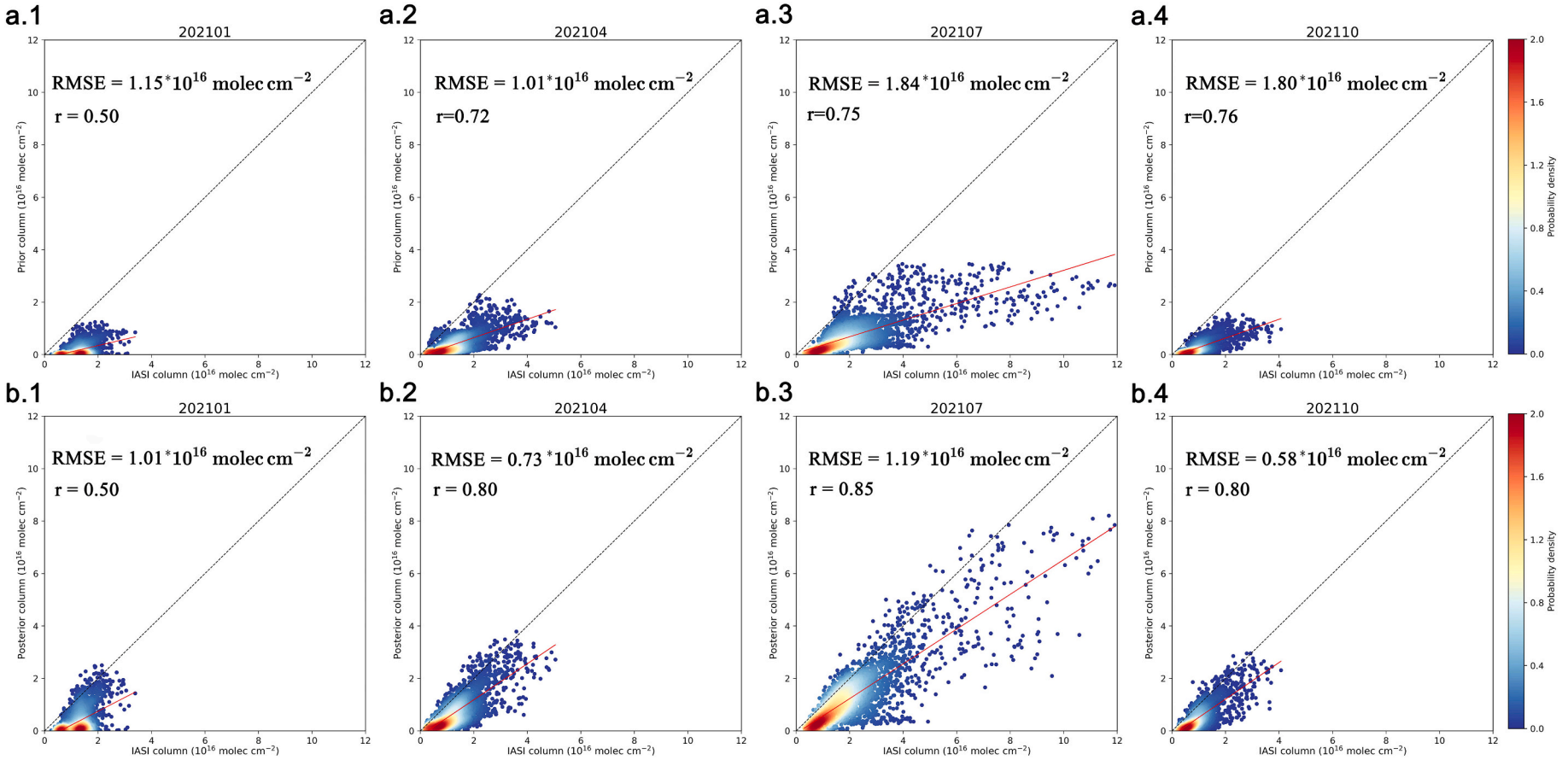

Fig. 2. Scatter plot of the observed vs. the simulated NH_3 total column concentration over China either using the prior (a) or using the posterior (b) NH_3 emission inventory in 2021 January (a.1)–(b.1), April (a.2)–(b.2), July(a.3)–(b.3) and October(a.4)–(b.4).

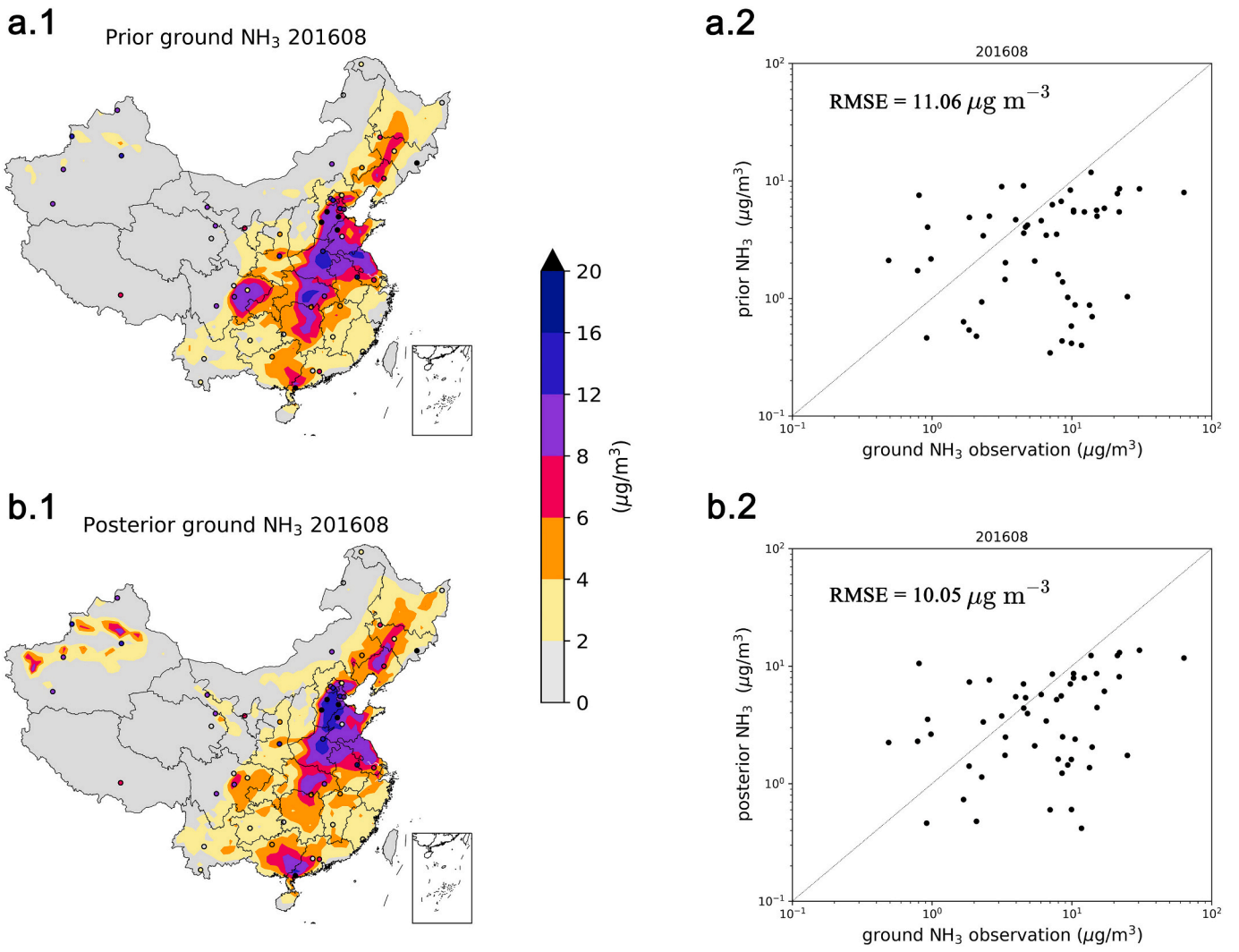

Fig. 3. Spatial distribution of the prior distribution (a) and the posterior (b) surface ammonia concentrations in August (a.1)–(b.1) 2016. Scatter plots of observed NH_3 surface concentrations versus prior simulation (a.2) and versus posterior simulation (b.2) collected in the corresponding months.

concentration distribution map at the four selected instants (Januray, April, July and October 2021). The CAMS global analysis, as a widely used product, undoubtedly demonstrates its value in multiple application fields. However, there is a significant deviation between the reanalysis results in certain regions and specific conditions and the actual situation compared to the observations. These deviations can be attributed to various factors such as the parameterization of the model, the emission data sources used, or the complexity of terrain and climate conditions. It should be emphasized that my reanalysis data is based on a wide range of datasets and advanced modeling techniques, and has undergone multiple rounds of validation and optimization to ensure its accuracy.

4. Result and discussion

Our reanalysis is the combination of the model simulation and satellite observations, and provides a more comprehensive and accurate reproduction of the atmospheric ammonia in China. Here the spatial pattern, monthly and annual variation of the Chinese ammonia features are explored with the newly developed reanalysis product in the follow part.

4.1. Spatial distribution

Fig. 6 plots the spatial pattern of the average atmospheric ammonia column concentration in the past decades, which shows significant regional differences. For the corresponding prior spatial distribution, please refer to Supplementary Fig. S1. It is obvious that NCP and SCB are the regions with highest ammonia affection exceeding 3.0×10^{16} molec cm^{-2}. Among them, NCP is characterized by heavy agricultural activities, especially high-intensity fertilizer application, which leads to a large amount of ammonia emission. Comparatively, the unique topography and meteorological conditions of the Sichuan Basin may have contributed to the accumulation of ammonia in this region, thus manifesting itself in higher concentrations (Zhang et al., 2010; Pan et al., 2018). In Xinjiang Province, there are typically moderate ammonia levels (0.5 to 1.5 $\times 10^{16}$ molec cm^{-2}) due to intensive agricultural activities. The nearby areas exhibited lower ammonia levels, attributable to less anthropogenic activities and colder environmental conditions. The central region of China tends to have higher ammonia concentrations (>1.5 $\times 10^{16}$ molec cm^{-2}), mainly driven by agricultural emissions. The southwest of China usually has lower levels, but some areas experience increased pollution due to a mix of industrial and agricultural activities. Cross-border pollution and transportation there also influence regional ammonia distribution in China. (Huang et al., 2012; Zhao et al., 2017).

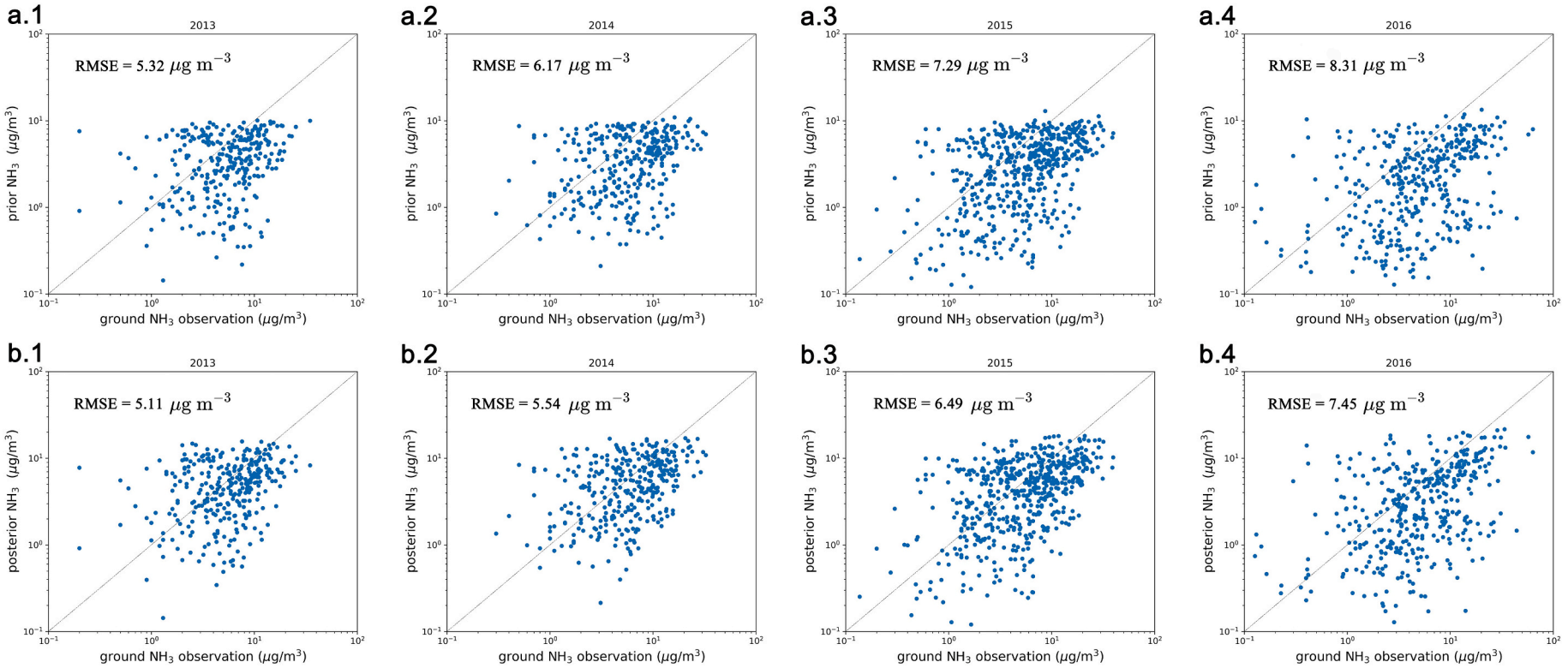

Fig. 4. Scatter plots compare observed NH_3 surface concentrations with a priori modeling results (a.1–a.4) and a posteriori modeling outcomes (b.1–b.4) for each year from 2013 to 2016.

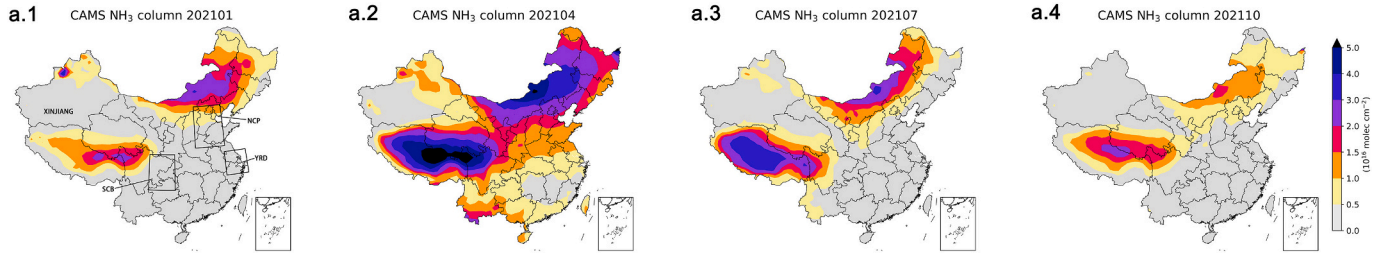

Fig. 5. Spatial distribution maps from the CAMS global reanalysis (EAC4) for (a.1) January, (a.2) April, (a.3) July, and (a.4) October 2021.

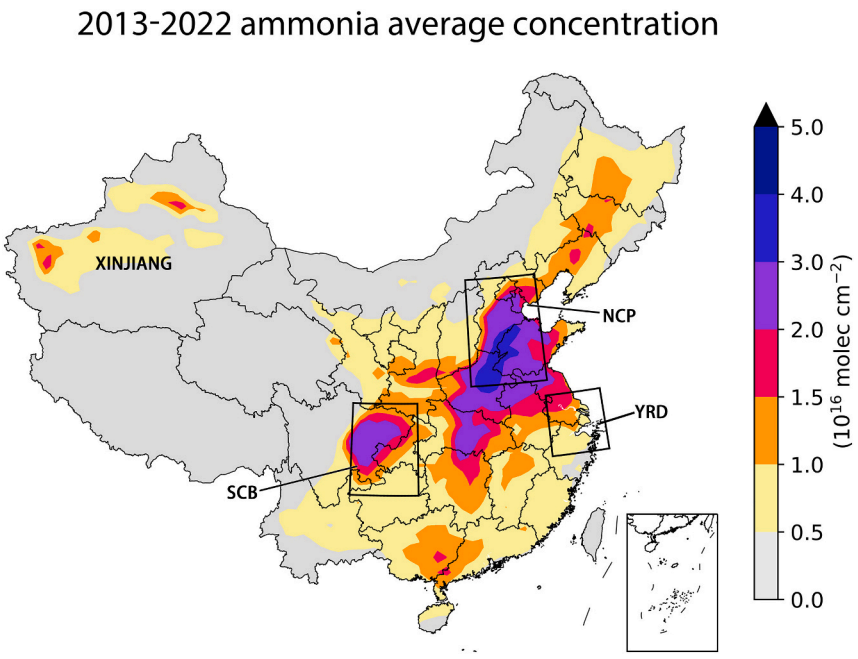

Fig. 6. Spatial distribution of the mean ammonia column concentration. The map presents the variations in average ammonia nitrogen levels across different regions of China from 2013 to 2022, highlighted with a clear color gradient. Essential study areas are marked for emphasis.

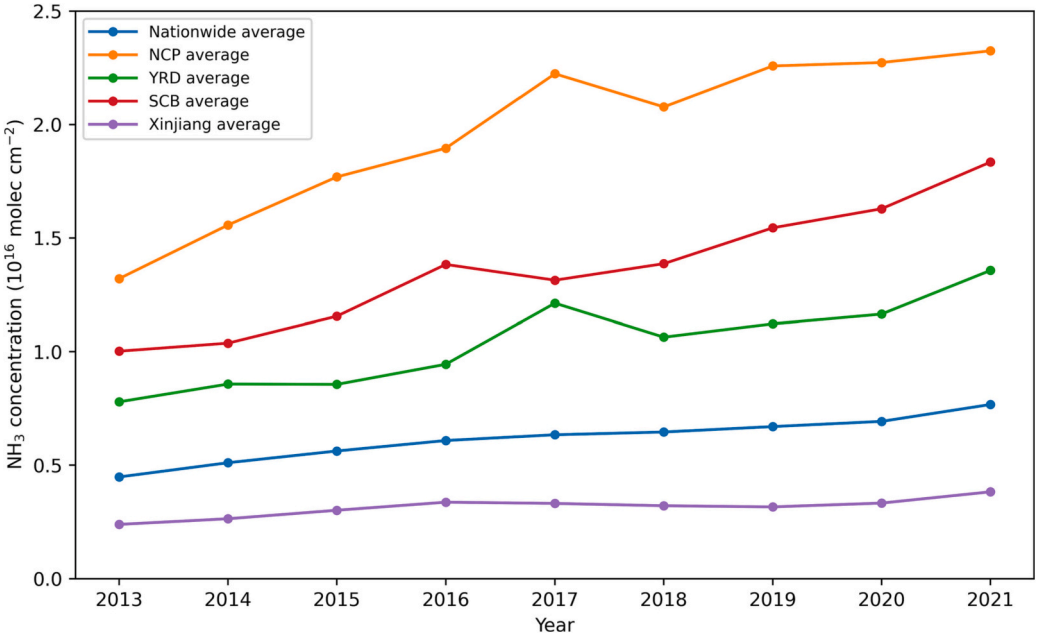

Fig. 7. Annual variations f the NH_3 column concentrations across China, NCP, YRD, SCB, and Xinjiang from 2013 to 2021. Distinct colors represent different regional averages.

4.2. Annual variation

Fig. 7 presents the temporal profiles of the national and regional (NCP, YRD, SCB and Xinjiang province) average ammonia column concentration spaning from 2013 to 2021. Reanalysis from July to December 2022 are not carried out because of absence of the newest IASI observations, therefore the average of 2022 is not present in this plot. Meanwhile, information about the varying trend in the prior simulation is provided in Supplementary Fig. S2. According to our assimilation results, the national atmospheric NH_3 concentration grows steadily from 0.45 to 0.77 $\times 10^{16}$ molec cm^{-2}, with a growth rate around 71.23 % in the past decade. As the most severe pollution region, NCP exhibited the most significant concentration growth, with a remarkable growth rate of 75.76 %. The atmospheric ammonia there increased rapidly from 1.32 to 2.32 $\times 10^{16}$ molec cm^{-2}, while most of these occurred in the period ranging from 2013 to 2017. Since 2008, agricultural growth has been the primary driver behind the increase in NH_3 emissions in China. This expansion in agriculture and the rising temperatures (Ding et al., 2007), has fostered the volatilization of NH_3, leading to heightened emissions from 2013 to 2017. Post-2017, NH_3 concentrations exhibit minor fluctuations (2.08–2.32 $\times 10^{16}$ molec cm^{-2}). This probably can be attributed to China's introduction of the "Opinions on Innovating System and Mechanisms to Promote Agricultural Green Development" in 2017, a significant initiative designed to foster sustainable and eco-friendly agricultural practices (less fertilizing) within the nation (Liu et al., 2020). Ammonia over SCB has the fastest ammonia growth ratio, 83 %, raising from 1.0 to 1.83 $\times 10^{16}$ molec cm^{-2}. Though there are also hotspots of atmospheric ammonia in Xinjiang province with local column concentration exceeding 1.5 $\times 10^{16}$ molec cm^{-2} as shown in Fig. 7, this is because the majority of the area consists of deserts, which are devoid of ammonia emissions. The mean column concentration there was about 0.25 $\times 10^{16}$ molec cm^{-2} in 2013, and slowly increased to 0.38 $\times 10^{16}$ molec cm^{-2} by 2021.

4.3. Monthly variation

Our newly-developed reanalysis is also capable of revealing the specific seasonal pattern at different regions. As shown in Fig. 8 are the monthly variation curve (solid line) and the spread (shadow) over the whole China and the four important regions. Meanwhile, information regarding the trend variations from the prior simulation is available in Supplementary Fig. S3. It indicates that the atmospheric ammonia peaks predominantly occur around June and August, while the lowest values are evident between December and January, and appeared in a normal distribution.

This is different from that found in European domain, which usually have the two peaks at Spring and Autumn, respectively (Backes et al., 2016). The varying profile is because that the emissions were primarily concentrated from April to September due to the intensive agricultural activities and high temperature. In China, the new spring seeding generally begins in April. During this period, spring wheat, soybeans, and cotton are sown in the single-cropping area with a large amount of N fertilizer applied to the cropland as the base fertilizer. In the following 1–2 months, due to the application of top fertilizer and warming air temperature, NH_3 emissions tend to continuously increase to August. Unlike the warm seasons, there is less volatilization of NH_3 during the winter season, and there is also relatively less farming activities. Therefore, the NH concentration decreases significantly compared to the summer season (Ren et al., 2023).

5. Summary and conclusion

Over the past few decades, the concentration of ammonia in China's atmosphere has steadily increased, giving rise to significant environmental and health concerns. Currently, obtaining a comprehensive understanding of China's atmospheric ammonia load and quantifying its environmental impact is a challenge. That cannot be adequately addressed solely through existing measurements or model simulations. These approaches are limited in terms of spatial coverage, data integrity, and quality, and thus fall short of meeting the necessary requirements. The conventional reanalysis products such as CAMS, despite their pivotal role in climate research, exhibit a marked deficiency in ammonia data, a lacuna that hampers our grasp of nitrogen cycles and atmospheric chemistry, particularly the aerosol formation processes.

This research has pioneered an integrated ammonia reanalysis data product in China, adeptly melding satellite observations from the IASI NH_3 dataset with model data, capitalizing on the robust EnKF data assimilation method. Ground based ammonia observations have been

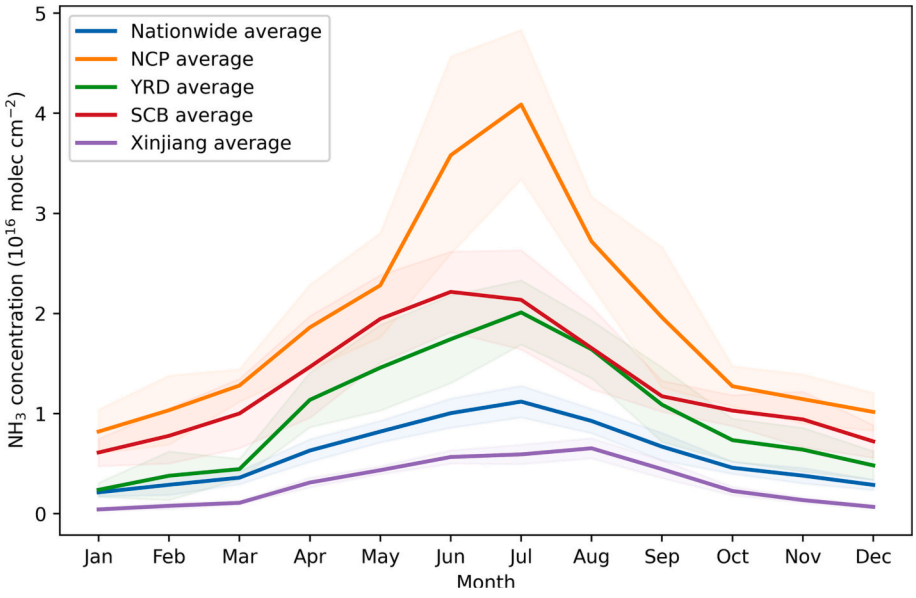

Fig. 8. Monthly variations of NH_3 concentrations across China, NCP, YRD, SCB, and Xinjiang in the past decade. The solid lines represent the monthly average NH_3 concentrations for each region, while the shaded areas depict the standard deviation of the annual averages, indicating the variability of the data. Each region is distinguished by a unique color.

used in the independent evaluation, and assured the high accuracy of our reanalysis. Spanning a decade from 2013 to 2022, this reanalysis uncovered not just the spatial intricacies of NH_3 concentrations but also their temporal dynamics. Notably, our findings pinpointed the spatial disparities in emission intensities, highlighting pronounced concentrations in the NCP, SCB, and Northeast China. The national atmospheric NH_3 concentration grew steadily from 0.45 to 0.77 $\times 10^{16}$ molec cm^{-2}. This represents an approximate growth rate of 71.23 % over the past decade. We also identified seasonal patterns, with peaks in July and reduced concentrations in winter. Our research provides crucial insights for shaping future NH_3 pollution prevention and control strategies in China.

Data availability

The IASI ANNI-NH_3-v3R-ERA5 data suites can be accessed at https://iasi.aeris-data.fr/. Meanwhile, the observed NH_3 concentration data (AMoN-China) has been published by Pan et al. (2018) from the Institute of Atmospheric Physics, Chinese Academy of Sciences.

CRediT authorship contribution statement

Bufan Xu: Formal analysis, Software, Writing – original draft. **Jianbing Jin:** Conceptualization, Funding acquisition, Methodology, Project administration, Writing – review & editing. **Li Fang:** Writing – review & editing. **Mijie Pang:** Writing – review & editing. **Ji Xia:** Writing – review & editing. **Baojie Li:** Writing – review & editing. **Hong Liao:** Supervision.

Declaration of competing interest

The authors declare that they have no known competing financial interests or personal relationships that could have appeared to influence the work reported in this paper.

Data availability

i have shared link to my data at the Attach file step

Acknowledgments

This work is supported by the National Natural Science Foundation of China [grant no. 42021004] and the Natural Science Foundation of Jiangsu Province (grant no. BK20210664 and BK20220031).

Appendix A. Supplementary data

Supplementary data to this article can be found online at https://doi.org/10.1016/j.scitotenv.2023.169053.

References

Backes, A.M., Aulinger, A., Bieser, J., Matthias, V., Quante, M., 2016. Ammonia emissions in Europe, part II: how ammonia emission abatement strategies affect secondary aerosols. Atmos. Environ. 126, 153–161.
Beer, R., Shephard, M.W., Kulawik, S.S., Clough, S.A., Eldering, A., Bowman, K.W., Sander, S.P., Fisher, B.M., Payne, V.H., Luo, M., et al., 2008. First satellite observations of lower tropospheric ammonia and methanol. Geophys. Res. Lett. 35.
Behera, S.N., Sharma, M., Aneja, V.P., Balasubramanian, R., 2013. Ammonia in the atmosphere: a review on emission sources, atmospheric chemistry and deposition on terrestrial bodies. Environ. Sci. Pollut. Res. 20, 8092–8131.
Bouillon, M., Safieddine, S., Hadji-Lazaro, J., Whitburn, S., Clarisse, L., Doutriaux-Boucher, M., Coppens, D., August, T., Jacquette, E., Clerbaux, C., 2020. Ten-year assessment of IASI radiance and temperature. Remote Sens. 12.
Clarisse, L., Clerbaux, C., Dentener, F., Hurtmans, D., Coheur, P.-F., 2009. Global ammonia distribution derived from infrared satellite observations. Nat. Geosci. 2, 479–483.
Clerbaux, C., Boynard, A., Clarisse, L., George, M., Hadji-Lazaro, J., Herbin, H., Hurtmans, D., Pommier, M., Razavi, A., Turquety, S., et al., 2009. Monitoring of atmospheric composition using the thermal infrared IASI/MetOp sounder. Atmos. Chem. Phys. 9, 6041–6054.
Compo, G.P., Whitaker, J.S., Sardeshmukh, P.D., Matsui, N., Allan, R.J., Yin, X., Gleason, B.E., Vose, R.S., Rutledge, G., Bessemoulin, P., et al., 2011. The twentieth century reanalysis project. Q. J. R. Meteorol. Soc. 137, 1–28.
Crippa, M., Guizzardi, D., Muntean, M., Schaaf, E., Dentener, F., Van Aardenne, J.A., Monni, S., Doering, U., Olivier, J.G., Pagliari, V., et al., 2018. Gridded emissions of air pollutants for the period 1970–2012 within EDGAR v4. 3.2. Earth Syst. Sci. Data 10, 1987–2013.
Dee, D.P., Uppala, S.M., Simmons, A.J., Berrisford, P., Poli, P., Kobayashi, S., Andrae, U., Balmaseda, M., Balsamo, G., Bauer, D.P., et al., 2011. The ERA-Interim reanalysis: configuration and performance of the data assimilation system. Q. J. Roy. Meteorol. Soc. 137, 553–597.
Ding, Y., Ren, G., Zhao, Z., Xu, Y., Luo, Y., Li, Q., Zhang, J., 2007. Detection, causes and projection of climate change over China: an overview of recent progress. Adv. Atmos. Sci. 24, 954–971.
Dong, J., Li, B., Li, Y., Zhou, R., Gan, C., Zhao, Y., Liu, R., Yang, Y., Wang, T., Liao, H., 2023. Atmospheric ammonia in China: long-term spatiotemporal variation, urban-rural gradient, and influencing factors. Sci. Total Environ. 883, 163–733.
Eastham, S.D., Weisenstein, D.K., Barrett, S.R., 2014. Development and evaluation of the unified tropospheric–stratospheric chemistry extension (UCX) for the global chemistry-transport model GEOS-Chem. Atmos. Environ. 89, 52–63.
Ebita, A., Kobayashi, S., Ota, Y., Moriya, M., Kumabe, R., Onogi, K., Harada, Y., Yasui, S., Miyaoka, K., Takahashi, K., Kamahori, H., Kobayashi, C., Endo, H., Soma, M., Oikawa, Y., Ishimizu, T., 2011. The Japanese 55-year reanalysis “JRA-55”: an interim report. SOLA 7, 149–152.
Evensen, G., 1994. Sequential data assimilation with a nonlinear quasi-geostrophic model using Monte Carlo methods to forecast error statistics. J. Geophys. Res. Oceans 99, 10,143–10,162.
Evensen, G., Vossepoel, F.C., van Leeuwen, P.J., 2022. Data Assimilation Fundamentals: A Unified Formulation of the State and Parameter Estimation Problem, Springer Textbooks in Earth Sciences, Geography and Environment. Springer International Publishing, Cham.
Franco, B., Clarisse, L., Stavrakou, T., Müller, J.-F., Pozzer, A., Hadji-Lazaro, J., Hurtmans, D., Clerbaux, C., Coheur, P.-F., 2019. Acetone atmospheric distribution retrieved from space. Geophys. Res. Lett. 46, 2884–2893.
Ge, X., Schaap, M., Kranenburg, R., Segers, A., Reinds, G.J., Kros, H., de Vries, W., 2020. Modeling atmospheric ammonia using agricultural emissions with improved spatial variability and temporal dynamics. Atmos. Chem. Phys. 20, 16,055–16,087.
Gelaro, R., McCarty, W., Suárez, M.J., Todling, R., Molod, A., Takacs, L., Randles, C.A., Darmenov, A., Bosilovich, M.G., Reichle, R., et al., 2017. The modern-era retrospective analysis for research and applications, version 2 (MERRA-2). J. Clim. 30, 5419–5454.
Hinzpeter, H., Kruspe, G., Wetzel, C., 2011. FGGE 1979 - First GARP Global Experiment.
Hoesly, R.M., Smith, S.J., Feng, L., Klimont, Z., Janssens-Maenhout, G., Pitkanen, T., Seibert, J.J., Vu, L., Andres, R.J., Bolt, R.M., et al., 2018. Historical (1750–2014) anthropogenic emissions of reactive gases and aerosols from the community emissions data system (CEDS). Geosci. Model Dev. 11, 369–408.
Houtekamer, P.L., Mitchell, H.L., 2001. A sequential ensemble Kalman filter for atmospheric data assimilation. Mon. Weather Rev. 129, 123–137.
Huang, X., Song, Y., Li, M., Li, J., Huo, Q., Cai, X., Zhu, T., Hu, M., Zhang, H., 2012. A high-resolution ammonia emission inventory in China. Glob. Biogeochem. Cycles 26.
Jacob, D.J., 1999. Introduction to Atmospheric Chemistry. Princeton university press.
Jin, J., Fang, L., Li, B., Liao, H., Wang, Y., Han, W., Li, K., Pang, M., Wu, X., Lin, H.X., 2023. 4DEnVar-based inversion system for ammonia emission estimation in China through assimilating IASI ammonia retrievals. Environ. Res. Lett. 18, 034 005.
Kalnay, E., 2002. Atmospheric Modeling, Data Assimilation and Predictability. Cambridge University Press.
Kalnay, E., Kanamitsu, M., Kistler, R., Collins, W., Deaven, D., Gandin, L., Iredell, M., Saha, S., White, G., Woollen, J., et al., 1996. The NCEP/NCAR 40-year reanalysis project. Bull. Am. Meteorol. Soc. 77, 437–472.
Kang, Y., Liu, M., Song, Y., Huang, X., Yao, H., Cai, X., Zhang, H., Kang, L., Liu, X., Yan, X., et al., 2016. High-resolution ammonia emissions inventories in China from 1980 to 2012. Atmos. Chem. Phys. 16, 2043–2058.
Lei, L., Anderson, J.L., 2014. Comparisons of empirical localization techniques for serial ensemble Kalman filters in a simple atmospheric general circulation model. Mon. Weather Rev. 142, 739–754.
Li, B., Chen, L., Shen, W., Jin, J., Wang, T., Wang, P., Yang, Y., Liao, H., 2021. Improved gridded ammonia emission inventory in China. Atmos. Chem. Phys. 21, 15,883–15,900.
Liu, H., Jacob, D.J., Bey, I., Yantosca, R.M., 2001. Constraints from 210Pb and 7Be on wet deposition and transport in a global three-dimensional chemical tracer model driven by assimilated meteorological fields. J. Geophys. Res. Atmos. 106, 12,109–12,128.
Liu, Y., Sun, D., Wang, H., Wang, X., Yu, G., Zhao, X., 2020. An evaluation of China's agricultural green production: 1978–2017. J. Clean. Prod. 243, 118–483.
Liu, P., Ding, J., Liu, L., Xu, W., Liu, X., 2022. Estimation of surface ammonia concentrations and emissions in China from the polar-orbiting infrared atmospheric sounding interferometer and the FY-4A geostationary interferometric infrared sounder. Atmos. Chem. Phys. 22, 9099–9110.
Liu, P., Chen, H., Song, Y., Xue, C., Ye, C., Zhao, X., Zhang, C., Liu, J., Mu, Y., 2023. Atmospheric ammonia in the rural North China Plain during wintertime: variations, sources, and implications for HONO heterogeneous formation. Sci. Total Environ. 861, 160–768. https://doi.org/10.1016/j.scitotenv.2022.160768.

Onogi, K., Tsutsui, J., Koide, H., Sakamoto, M., Kobayashi, S., Hatsushika, H., Matsumoto, T., Yamazaki, N., Kamahori, H., Takahashi, K., et al., 2007. The JRA-25 reanalysis. J. Meteorol. Soc. Japan Ser. II (85), 369–432.
Pan, Y., Tian, S., Zhao, Y., Zhang, L., Zhu, X., Gao, J., Huang, W., Zhou, Y., Song, Y., Zhang, Q., et al., 2018. Identifying ammonia hotspots in China using a national observation network. Environ. Sci. Technol. 52, 3926–3934.
Park, R.J., Jacob, D.J., Field, B.D., Yantosca, R.M., Chin, M., 2004. Natural and transboundary pollution influences on sulfate-nitrate-ammonium aerosols in the United States: implications for policy. J. Geophys. Res. Atmos. 109.
Paulot, F., Jacob, D.J., Johnson, M.T., Bell, T.G., Baker, A.R., Keene, W.C., Lima, I.D., Doney, S.C., Stock, C.A., 2015. Global oceanic emission of ammonia: constraints from seawater and atmospheric observations. Glob. Biogeochem. Cycles 29, 1165–1178.
Ren, C., Huang, X., Liu, T., Song, Y., Wen, Z., Liu, X., Ding, A., Zhu, T., 2023. A dynamic ammonia emission model and the online coupling with WRF–Chem (WRF–SoilN–Chem v1.0): development and regional evaluation in China. Geosci. Model Dev. 16, 1641–1659.
Rienecker, M.M., Suarez, M.J., Gelaro, R., Todling, R., Bacmeister, J., Liu, E., Bosilovich, M.G., Schubert, S.D., Takacs, L., Kim, G.-K., et al., 2011. MERRA: NASA's modern-era retrospective analysis for research and applications. J. Clim. 24, 3624–3648.
Saha, S., Moorthi, S., Pan, H.-L., Wu, X., Wang, J., Nadiga, S., Tripp, P., Kistler, R., Woollen, J., Behringer, D., et al., 2010. The NCEP climate forecast system reanalysis. Bull. Am. Meteorol. Soc. 91, 1015–1058.
Shephard, M., Cady-Pereira, K., 2015. Cross-track infrared sounder (CrIS) satellite observations of tropospheric ammonia. Atmos. Meas. Tech. 8, 1323–1336.
Sutton, M., Fowler, D., 2002. Introduction: fluxes and impacts of atmospheric ammonia on national, landscape and farm scales. Environ. Pollut. 119, 7–8.
Sutton, M.A., Erisman, J.W., Dentener, F., Möller, D., 2008. Ammonia in the environment: from ancient times to the present. Environ. Pollut. 156, 583–604.
Ti, C., Xia, L., Chang, S.X., Yan, X., 2019. Potential for mitigating global agricultural ammonia emission: a meta-analysis. Environ. Pollut. 245, 141–148.
Van Damme, M., Whitburn, S., Clarisse, L., Clerbaux, C., Hurtmans, D., Coheur, P.-F., 2017. Version 2 of the IASI NH 3 neural network retrieval algorithm: near-real-time and reanalysed datasets. Atmos. Meas. Tech. 10, 4905–4914.
Walker, J., Philip, S., Martin, R., Seinfeld, J., 2012. Simulation of nitrate, sulfate, and ammonium aerosols over the United States. Atmos. Chem. Phys. 12, 11,213–11,227.
Wang, C., Yin, S., Bai, L., Zhang, X., Gu, X., Zhang, H., Lu, Q., Zhang, R., 2018. High-resolution ammonia emission inventories with comprehensive analysis and evaluation in Henan, China, 2006–2016. Atmos. Environ. 193, 11–23.
Warner, J.X., Wei, Z., Strow, L.L., Dickerson, R.R., Nowak, J.B., 2016. The global tropospheric ammonia distribution as seen in the 13-year AIRS measurement record. Atmos. Chem. Phys. 16, 5467–5479.
Wesely, M., 2007. Parameterization of surface resistances to gaseous dry deposition in regional-scale numerical models. Atmos. Environ. 41, 52–63.
Xu, W., Luo, X., Pan, Y., Zhang, L., Tang, A., Shen, J., Zhang, Y., Li, K., Wu, Q., Yang, D., et al., 2015. Quantifying atmospheric nitrogen deposition through a nationwide monitoring network across China. Atmos. Chem. Phys. 15, 12,345–12,360.
Xu, P., Liao, Y., Lin, Y., Zhao, C., Yan, C., Cao, M., Wang, G., Luan, S., 2016. High-resolution inventory of ammonia emissions from agricultural fertilizer in China from 1978 to 2008. Atmos. Chem. Phys. 16, 1207–1218.
Zhan, X., Adalibieke, W., Cui, X., Winiwarter, W., Reis, S., Zhang, L., Bai, Z., Wang, Q., Huang, W., Zhou, F., 2020. Improved estimates of ammonia emissions from global croplands. Environ. Sci. Technol. 55, 1329–1338.
Zhang, L., Gong, S., Padro, J., Barrie, L., 2001. A size-segregated particle dry deposition scheme for an atmospheric aerosol module. Atmos. Environ. 35, 549–560.
Zhang, Y., Dore, A., Ma, L., Liu, X., Ma, W., Cape, J., Zhang, F., 2010. Agricultural ammonia emissions inventory and spatial distribution in the North China Plain. Environ. Pollut. 158, 490–501.
Zhang, L., Chen, Y., Zhao, Y., Henze, D.K., Zhu, L., Song, Y., Paulot, F., Liu, X., Pan, Y., Lin, Y., et al., 2018. Agricultural ammonia emissions in China: reconciling bottom-up and top-down estimates. Atmos. Chem. Phys. 18, 339–355.
Zhang, S., Li, D., Ge, S., Liu, S., Wu, C., Wang, Y., Chen, Y., Lv, S., Wang, F., Meng, J., Wang, G., 2021. Rapid sulfate formation from synergetic oxidation of SO2 by O3 and NO2 under ammonia-rich conditions: implications for the explosive growth of atmospheric PM2.5 during haze events in China. Sci. Total Environ. 772, 144–897.
Zhao, Y., Zhang, L., Chen, Y., Liu, X., Xu, W., Pan, Y., Duan, L., 2017. Atmospheric nitrogen deposition to China: a model analysis on nitrogen budget and critical load exceedance. Atmos. Environ. 153, 32–40.
Zhou, F., Ciais, P., Hayashi, K., Galloway, J., Kim, D.-G., Yang, C., Li, S., Liu, B., Shang, Z., Gao, S., 2016. Re-estimating NH3 emissions from Chinese cropland by a new nonlinear model. Environ. Sci. Technol. 50, 564–572.